

Organic Photovoltaics

Regulate the Singlet–Triplet Energy Gap by Spatially Separating HOMO and LUMO for High Performance Organic Photovoltaic Acceptors

Guangkun Song⁺, Tengfei He⁺, Ruohan Wang, Yanni Ouyang, Nakul Jain, Saisai Liu, Bin Kan, Yujie Shang, Jiaqi Li, Xingkai Wang, Zhaoyang Yao, Xiangjian Wan, Chenxi Li, Wei Ma, Yan Zhao, Guankui Long,* Chunfeng Zhang,* Feng Gao, and Yongsheng Chen*

Abstract: Reducing the single-triplet energy gap (ΔE_{ST}) for organic photovoltaic (OPV) molecules has been proposed to be able to reduce the nonradiative recombination by tuning the low-lying triplet state (T_1) and/or the excited state (S_1), thus reducing the energy loss (E_{loss}) and increasing the open-circuit voltage in their devices. However, how to design the non-fullerene acceptor (NFA) with small ΔE_{ST} and high performance is challenging. Aiming to address this issue, **YDF**, **YTF**, and **YTF-H** were synthesized. Among them, a device based on **YDF** with partially spatially separated highest occupied molecular orbital (HOMO) and lowest unoccupied molecular orbital (LUMO) exhibits a much higher power conversion efficiency (PCE) of 20.04%, which is one of the most efficient efficiencies for binary systems. For **YTF** and **YTF-H**, their completely spatially separated HOMO and LUMO indeed lead to a much reduced ΔE_{ST} caused by the low-lying S_1 state, together with excellent charge mobility and light absorption, required for higher performance OPV. But their low S_1 state causes several non-radiative recombinations due to strong S_1 - S_0 coupling (PCE < 1.5%). These results indicate that future designs to have high performance molecules with small ΔE_{ST} should avoid the sharp decrease in S_1 , and the ideal scenario would be to elevate the T_1 state, thereby mitigating the energy gap law.

Introduction

Organic photovoltaics (OPVs), as promising candidates for renewable energy technologies, have progressed rapidly to achieve the power conversion efficiency (PCE) of over 20%^[1–9] via delicate molecular design and device engineering based on non-fullerene acceptors (NFAs). However, the performance of OPVs is still less than the perovskite solar cells (PSCs), which have shown a PCE above 26%.^[10,11] The main limiting factor for OPV performance is the larger energy loss (E_{loss}) between the material band gap (E_g) and device open-circuit voltage (V_{OC} , $E_{loss} = E_g -$

eV_{OC}).^[12] For optimized PSCs, the E_{loss} can be as low as 0.34 eV, while for state-of-the-art OPVs, the E_{loss} typically is in the range between 0.5 and 0.6 eV.^[13,14] From a molecular perspective, OPV materials exhibit larger defects, stronger lattice vibrations, and more other energetic disorder compared to perovskites and Si-based solar materials, which contribute to intrinsic strong electron-phonon coupling between the states of S_1/CT with S_0 state.^[15] These inherent properties caused a larger non-radiative voltage loss (ΔV_{nr}) in OPVs, ranging from 0.2 to 0.4 eV.^[13] The ΔV_{nr} is intrinsically linked to the external electroluminescence quantum efficiency (EQE_{EL}) of the device based on

[*] G. Song⁺, T. He⁺, R. Wang, S. Liu, Y. Shang, J. Li, X. Wang, Z. Yao, X. Wan, C. Li, Y. Chen
State Key Laboratory and Institute of Elemento-Organic Chemistry, The Centre of Nanoscale Science and Technology and Key Laboratory of Functional Polymer Materials, Renewable Energy Conversion and Storage Center (RECAST), Frontiers Science Center for New Organic Matter, College of Chemistry, Nankai University, Tianjin 300071, China
E-mail: yschen99@nankai.edu.cn

T. He⁺, B. Kan, G. Long
School of Materials Science and Engineering, National Institute for Advanced Materials, Nankai University, Tianjin 300350, China
E-mail: longgk09@nankai.edu.cn

Y. Ouyang, C. Zhang
National Laboratory of Solid-State Microstructures, School of Physics, and Collaborative Innovation Center for Advanced


Microstructures, Nanjing University, Nanjing 210093, China
E-mail: cfzhang@nju.edu.cn

W. Ma
State Key Laboratory for Mechanical Behavior of Materials, Xi'an Jiaotong University, Xi'an 710049, China

Y. Zhao
Department of Materials Science, Fudan University, Shanghai 200433, China

N. Jain, F. Gao
Department of Physics Chemistry and Biology (IFM), Linköping University, Linköping, Sweden

[†] Both authors contributed equally to this work.

 Additional supporting information can be found online in the Supporting Information section

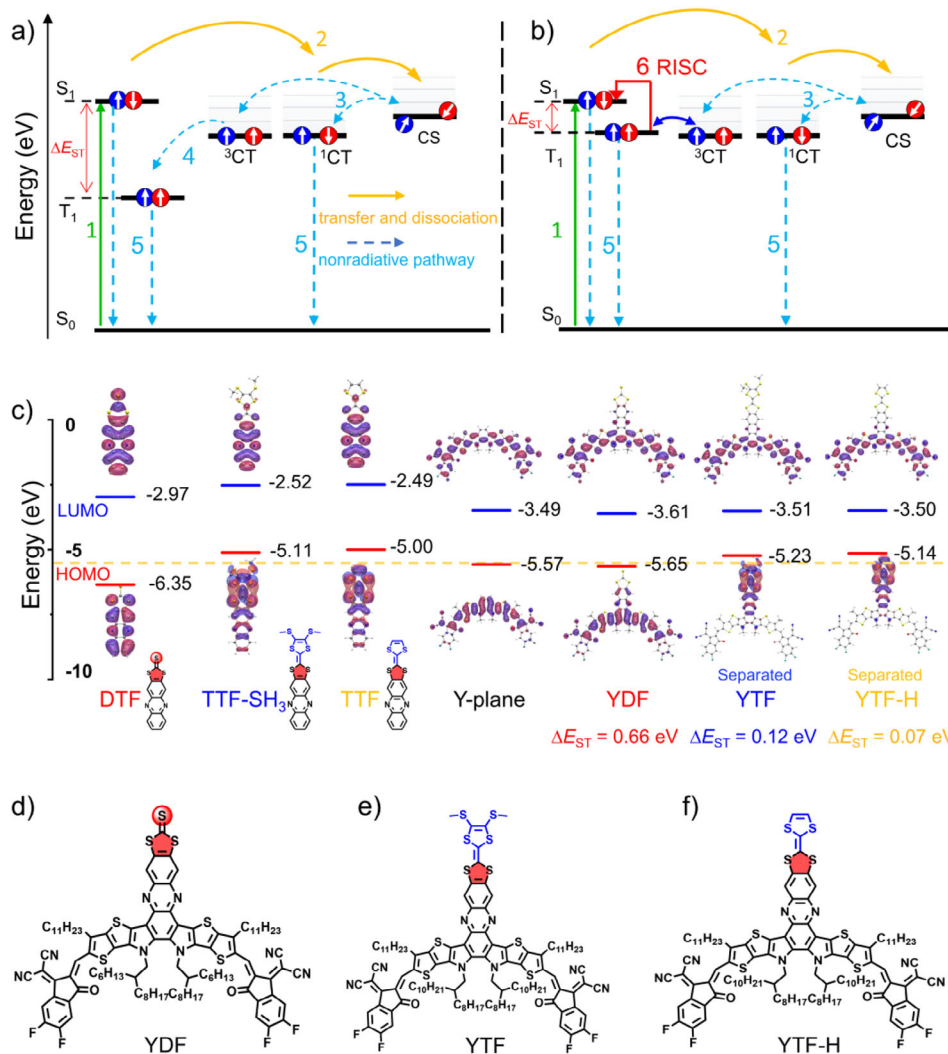


Figure 1. a) State diagram representing the various photophysical processes in an OPV. b) Ideal photophysical process. Reducing the ΔE_{ST} by elevating the T₁ state. c) Calculated frontier molecular orbital energy levels and distributions of the investigated fragments and molecules. d)–f) Molecular structures of YDF, YTF, and YTF-H.

Equation (1),^[16]

$$\Delta V_{nr} = -\frac{k_B T}{e} \ln(\text{EQE}_{EL}) \quad (1)$$

while EQE_{EL} is related to both the radiative (k_r) and non-radiative recombination rate constants (k_{nr} , Equation 2).

$$\text{EQE}_{EL} \propto \frac{k_r}{k_r + k_{nr}} \quad (2)$$

In most OPVs that use NFAs, the majority of charge recombination under open-circuit conditions proceeds via the formation of non-radiative NFA triplet excitons.^[17] Therefore, decreasing the k_{nr} by reducing the coupling of S₁/T₁ with S₀ and the defects could increase the EQE_{EL} and then reduce the ΔV_{nr} .^[18] In OPVs, the large ΔE_{ST} , around 0.6–1.0 eV for either donor or acceptor materials, makes T₁ excitons hard to be thermally re-dissociated into free charges and has to decay

non-radiatively, resulting in the large ΔV_{nr} ^[18] (as shown in Figure 1a). Furthermore, smaller ΔE_{ST} could also recycle the T₁ exciton to the S₁ exciton through the reversed intersystem crossing (RISC, Figure 1b).

$$\Delta E_{ST} = S_1 - T_1 \approx 2J \quad (3)$$

$$J = \iint \phi_{\text{HOMO}}(r_1) \phi_{\text{LUMO}}(r_2) \frac{1}{|r_1 - r_2|} \phi_{\text{HOMO}}(r_2) \phi_{\text{LUMO}}(r_1) dr_1 dr_2 \quad (4)$$

From quantum mechanics, the ΔE_{ST} is approximately twice the value of the exchange integral (J , Equations 3 and 4) between the spatial wavefunctions of the highest occupied molecular orbital (HOMO) and the lowest unoccupied molecular orbital (LUMO).^[19] Therefore, ΔE_{ST} will be reduced by decreasing the overlap of HOMO and LUMO ($\int \phi_{\text{HOMO}} \phi_{\text{LUMO}} dr$) and increasing the spatial distance $|r_1 - r_2|$.

This can likely be achieved through two paths: (1) spatially separating the HOMO and LUMO (increasing $|r_1-r_2|$), such as that in 4CzPN, etc.;^[20] (2) having an overall orthogonal distribution of HOMO and LUMO orbitals ($\int \phi_{\text{HOMO}}\phi_{\text{LUMO}}dr$) as such as in many B,N polycyclic aromatic hydrocarbons^[21] or the extreme case of that between the electron orbitals of $P_x/P_y/P_z$ in a carbon atom. Indeed, these approaches have been widely used in constructing the highly efficient thermally activated delayed fluorescence (TADF) emitters and achieved <0.2 eV of ΔE_{ST} .^[22]

However, conventional TADF materials with small ΔE_{ST} are unfavorable for OPVs, as they could not achieve strong light absorption and effective charge transport due to their twisted Donor–Acceptor (D–A) geometries and less π -overlapped packing mode.^[23] Thus, designing OPV molecules with reduced ΔE_{ST} while maintaining the necessary properties of strong light absorption and high charge mobility presents a significant challenge.

Herein, aiming to address this issue, a frontier molecular orbital engineering (FMOE) strategy to reduce ΔE_{ST} by spatially separating HOMO and LUMO in the most typical best performance A–D–A structure acceptors (such as Y6^[24] and CH-series^[25]) was proposed and explored. Through screening the representative fragments based on theoretical calculation, we found that the tetrathiafulvalene (TTF) unit exhibits a much higher HOMO than the Y-plane; thus, the integration of the TTF unit with the Y6 backbone could render the HOMO localized on the TTF unit, while the LUMO still mainly keeps spatially on the Y-backbone. Therefore, the HOMO and LUMO could be spatially separated, and correspondingly decreased ΔE_{ST} can be achieved on these typical NFAs. With this, three novel NFAs based on the TTF unit, **YDF**, **YTF**, and **YTF-H**, were designed and synthesized. As expected, **YDF**, **YTF**, and **YTF-H** still maintain excellent light absorption capacity and charge transport mobility. Among them, indeed as expected, molecules **YTF** and **YTF-H** have achieved spatially HOMO and LUMO separated largely, resulting in a much smaller ΔE_{ST} of 0.12 and 0.06 eV, respectively, together with highly kept strong absorption and high mobility (see below). However, the much reducing of ΔE_{ST} was manifested by a significantly low-lying S_1 state, which results in almost completely quenched fluorescence with marked enhancement of non-radiative recombination and thus poor PCE of $<1.5\%$. But for the control acceptor **YDF**, its HOMO and LUMO only exhibit partial separation, still similar to that in the case of Y6 and CH-series molecules, with ΔE_{ST} at the comparable value of 0.66 eV but a much higher binary PCE of 20.04%.

With these results, we conclude that reducing the ΔE_{ST} with spatially separated HOMO and LUMO by decreasing S_1 is not a good approach and the ideal scenario might be to elevate the T_1 state (Figure 1b), thereby mitigating the non-radiative processes caused by the energy gap law. The likely best strategy to achieve such a goal for acceptors should have at least the following rules simultaneously: (1) high-lying T_1 state, (2) HOMO and LUMO separated spatially or distributed orthogonally, and (3) strong absorption and charge mobility.

Results and Discussion

Synthesis of Acceptors with Separated HOMO–LUMO

To construct NFAs with small ΔE_{ST} , we employed an FMOE strategy to achieve the HOMO and LUMO wave function separation. Through screening the representative fragments based on theoretical calculation (Figures S1 and S2), we found that only the TTF-based unit (-5.00 eV) exhibits a much higher HOMO than the Y6-plane (-5.57 eV). Therefore, the combination of TTF derivatives with the Y6-plane could fulfill the aim of regulating the HOMO and LUMO distribution and thus decreasing ΔE_{ST} . The calculated HOMO results for the derivatives DTF (dithiafulvalene, -6.35 eV), TTF (-5.00 eV), and TTF-SCH₃ (-5.11 eV) were shown in Figure 1c. Note, the HOMO of DTF is much lower, which could not satisfy the requirement of HOMO and LUMO separation. Therefore, according to our previous strategy,^[12] three NFAs based on the derivatives DTF, TTF-SCH₃, and TTF **YDF**, **YTF**, and **YTF-H** were synthesized through NH–NH₂ condensation (Figure 1d–f). As expected, the HOMO of **YTF** and **YTF-H** are localized at the central donor core, and that of **YDF** is delocalized on the conjugated Y-plane (Figure 1c). All these three NFAs exhibit a similar LUMO distribution on the Y-plane. The overlap integral between HOMO and LUMO ($O_{\text{H/L}}$) for **YTF** and **YTF-H** is as low as 0.14 a.u. (Figures 2e and S4), respectively, while for **YDF** it is 0.68 a.u. Therefore, the spatially separated HOMO and LUMO lead to the ΔE_{ST} of **YTF** and **YTF-H** sharply decreasing to 0.12 and 0.07 eV, respectively, while the ΔE_{ST} of **YDF** still remains at 0.66 eV. On the other hand, the overlap integral between HOMO–1 and LUMO ($O_{\text{H-1/L}}$) for **YTF** and **YTF-H** is 0.67 and 0.66 a.u., respectively, which is almost the same as the $O_{\text{H/L}}$ for **YDF**. In order to understand the origin of this, the HOMO–1, HOMO, and LUMO energy levels of these three NFAs were systematically investigated by cyclic voltammetry (CV), UV–vis absorption spectra, and theoretical calculations as shown below.

Photophysical Properties and Photovoltaic Performance

To understand the electronic levels and the photo-physical properties of the materials, CV measurements were performed (Figures 2a and S6). It is noted that **YTF** and **YTF-H** exhibit distinct peaks within the range of -2000 – 2000 mV. The introduction of the strong electron-donating central core (TTF and TTF-SCH₃) notably elevated the HOMO level of **YTF** (-5.20 eV) and **YTF-H** (-5.16 eV) compared to that of **YDF** (-5.65 eV), and the additional peaks of HOMO–1 for **YTF** (-5.54 eV) and **YTF-H** (-5.55 eV) were observed. As summarized in Table 1, the energy difference between HOMO and LUMO ($\Delta E_{\text{HOMO-LUMO}}$) of **YTF** (1.42 eV) and **YTF-H** (1.40 eV) was clearly lower than that of **YDF** (1.82 eV). It is surprising to find that the energy difference between HOMO–1 and LUMO ($\Delta E_{\text{HOMO-1-LUMO}}$) of **YTF** (1.80 eV) and **YTF-H** (1.79 eV) is similar to the $\Delta E_{\text{HOMO-LUMO}}$ of **YDF**. Further, the absorption spectra

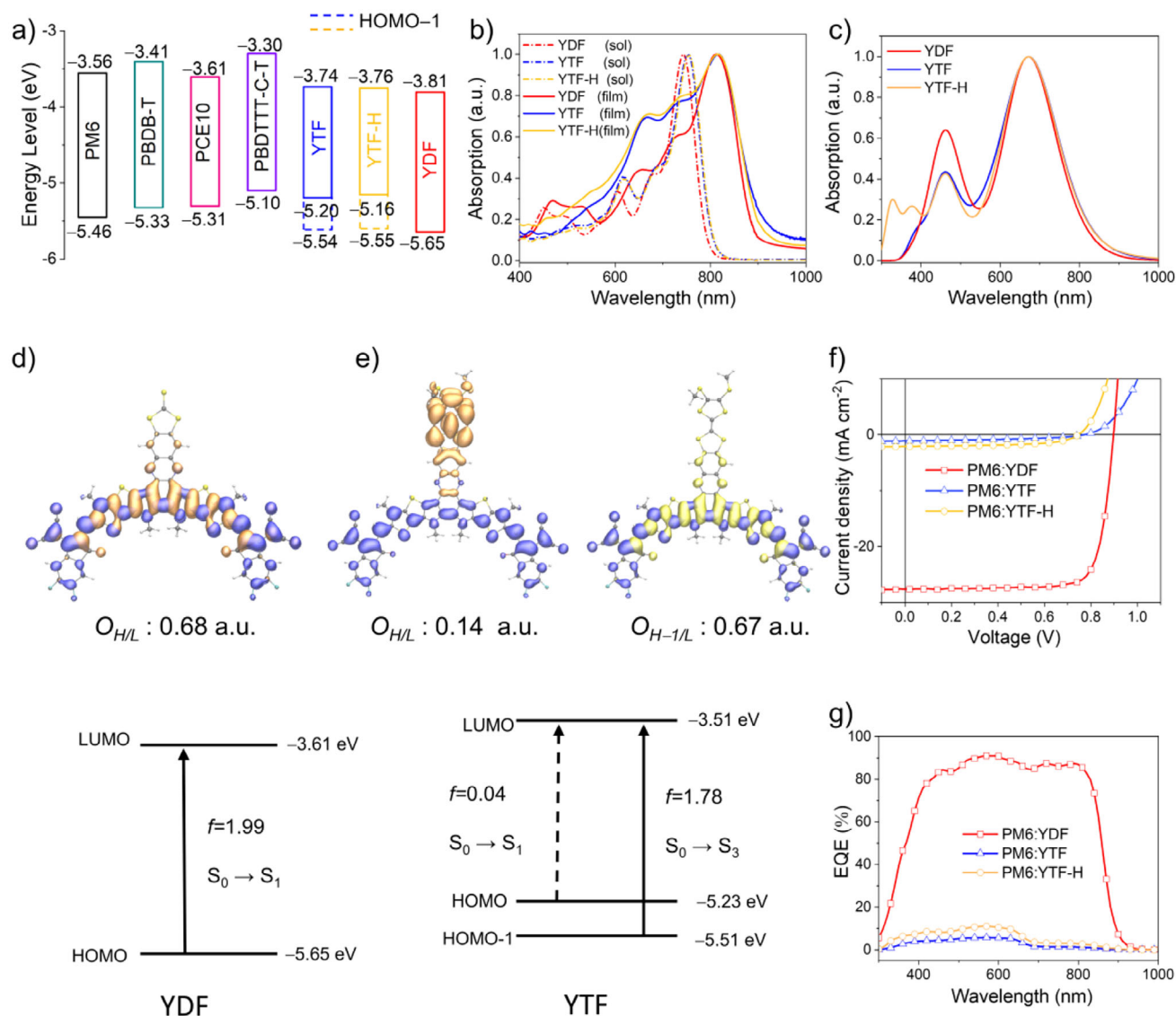


Figure 2. a) Energy level diagram of the donors and acceptors. b) Normalized absorption spectra of acceptors in diluted solutions of chloroform and neat films. c) the theoretically calculated UV-vis absorption spectra of **YDF**, **YTF**, and **YTF-H**. d) and e) TD-DFT calculated molecular orbitals and energy diagrams at the B3LYP/6-31G. $O_{H/L}$ represents the overlap integral between HOMO and LUMO, and f represents the oscillator strength. f) J-V characteristics of the best-performing cells of binary PM6/acceptors. g) External quantum efficiency (EQE) spectra.

Table 1: Optical properties and electronic energy levels of **YDF**, **YTF**, and **YTF-H**.

Comp.	LUMO (eV)	HOMO-1 (eV)	HOMO (eV)	$\Delta E_{\text{HOMO} \sim \text{LUMO}}$ (eV)	$\Delta E_{\text{HOMO-1} \sim \text{LUMO}}$ (eV)	$\lambda_{\text{MAX}}^{\text{Sol}}$ (nm)	$\lambda_{\text{MAX}}^{\text{Film}}$ (nm)	$E_{\text{g}}^{\text{Opt}}$ (eV) ^{b)}
YDF	-3.81	\	-5.64	1.82	\	741	812	1.39
YTF	-3.74	-5.54	-5.20	1.42	1.80	754	818	1.35
YTF-H	-3.76	-5.55	-5.16	1.40	1.79	754	820	1.37

of **YDF**, **YTF**, and **YTF-H** in chloroform and neat films (Figure 2b) are measured. The main absorption peaks (741 for **YDF**, 754 for **YTF** and 754 nm for **YTF-H** in Table 1), molar extinction coefficients ($2.51 \times 10^5 \text{ M}^{-1} \text{ cm}^{-1}$ for **YDF**, $1.92 \times 10^5 \text{ M}^{-1} \text{ cm}^{-1}$ for **YTF** and $2.27 \times 10^5 \text{ M}^{-1} \text{ cm}^{-1}$ for **YTF-H**), and optical bandgap ($E_{\text{g}}^{\text{opt}}$) of **YDF**, **YTF**, and **YTF-H** are found to be very similar. Therefore, the separation

of HOMO and LUMO of **YTF** and **YTF-H** does not diminish their light absorption capabilities. To elucidate the underlying mechanisms, a comprehensive theoretical analysis was systematically conducted.

The theoretical absorption spectra of **YDF**, **YTF**, and **YTF-H** were calculated based on the time-dependent density functional theory (TD-DFT) and shown in Figure 2c, which

Table 2: Photovoltaic performance parameters of OPVs based on **PM6: YDF**, **PM6: YTF**, and **PM6: YTF-H** and measured under the illumination of AM 1.5G (100 mW cm⁻²).^{a)}

Active layer	V _{OC} (V)	J _{SC} (mA cm ⁻²)	J _{SC} ^{cal} ^{b)} (mA cm ⁻²)	FF (%)	PCE (%)
PM6: YTF	0.773	1.12	1.06	43.17	0.37
PBDB-T: YTF	0.634	1.77	\	38.38	0.43
PCE-10: YTF	0.615	1.55	\	38.58	0.37
PBDTTT-C-T: YTF	0.678	5.33	\	36.99	1.33
PM6: YTF-H	0.745	1.75	2.07	50.83	0.66
PM6: YDF	0.901(0.898 ± 0.002)	27.70(27.75 ± 0.14)	26.72	80.40(80.10 ± 0.36)	20.04(19.96 ± 0.05)

^{a)} The values in parentheses are average parameters obtained from the top 10 best devices. ^{b)} The J_{SC}^{cal} is determined from integration of the EQEs to the AM1.5G spectrum.

are consistent with the experimentally measured results. The maximum absorption peak of **YDF** (S₀→S₁ transition at 674.30 nm, Table S1) involves the main contribution from HOMO→LUMO transition (oscillator strength $f = 1.99$), which is characterized as the localized excitation (LE). In contrast, the S₀→S₁ absorption for **YTF** and **YTF-H** shows a relatively weak oscillator strength (816.93 nm, $f = 0.04$), which is characterized as the charge transfer (CT) from the electron-deficient core (TTF unit) to the Y-plane. This is consistent with the design principle of achieving HOMO and LUMO separation of **YTF** and **YTF-H** as discussed above. More importantly, **YTF** exhibit a very strong S₀→S₃ transition (679.69 nm, $f = 1.78$), which mainly involves the HOMO-1→LUMO with clear LE character (Figure 2e). This large difference between the oscillator strength of HOMO→LUMO and HOMO-1→LUMO transitions of **YTF** and **YTF-H** makes the S₀→S₁ absorption is optically dark while the S₀→S₃ absorption optically bright.^[26] Therefore, the absorption range and intensity of **YTF** and **YTF-H** are not sacrificed even when the HOMO and LUMO are separated. This is also consistent with the energy levels of CV measurements as discussed above (Table 1).

Furthermore, our molecular design principle enables **YTF** and **YTF-H** to achieve both high hole and electron mobilities with the order of 10⁻⁴ cm² V⁻¹ s⁻¹, similar to **YDF** and other NFAs (Figure S12). In contrast to traditional TADF materials,^[27] **YTF** and **YTF-H** do not sacrifice the absorption intensity and charge transport property upon HOMO-LUMO separation and have not been reported/explored before.

The grazing-incidence wide-angle X-ray scattering (GIWAXS) is then performed to investigate the packing information of **YDF**, **YTF**, and **YTF-H**. It is found that **YDF**, **YTF**, and **YTF-H** based films possess the preferential face-on orientations supported by strong (010) π - π stacking peaks in the out-of-plane direction. Besides, in the neat films, all acceptors exhibit basically consistent stacking distances and coherence lengths (CLs) in the (100) and (010) directions (Table S3 and Figures S9 and S10). Therefore, there is negligible difference between the molecular packing of **YDF**, **YTF**, and **YTF-H**. The similar CCL trend is also observed in their blend films, implying **YDF**, **YTF**, and **YTF-H** gained an ordered and similar packing when blended with **PM6**. The atomic force microscopy-based infrared spectroscopy (AFM-IR) was also measured and shown in Figure S11; all blended films exhibit a similar and smooth surface morphology.

Through single-crystal X-ray diffraction (SC-XRD) analysis, **YDF** and **YTF**^[28] exhibit similar stacking modes, and both form effective three-dimensional interpenetrating networks (Figures S21–S28) with the corresponding molecular packing density (MPD) of 64.8% and 63.0%, respectively.

Although **YDF**, **YTF**, and **YTF-H** can effectively absorb within a similar range and exhibit comparable packing in neat and blended films, their device performance differs by dozens of times (Table 2). Extremely inferior photovoltaic response has been observed for **YTF** and **YTF-H** based devices regardless of the usage of different polymer donors. The very similar molecular packing and morphology (as described above) results indicate that the significant performance difference among these molecules in OPV should come from other reasons. Considering the issue of energy level matching, **PBDTTT-C-T** with a high HOMO energy level as the donor was also employed, which increased the J_{sc} to 5.33 mA cm⁻², but the device efficiency was still poor (1.33%). Therefore, energy level matching is neither the main factor for the low performance of **YTF** and **YTF-H**. In contrast, the optimized **YDF**-based device offers a remarkable PCE of 20.04%, with a high EQE of ~85% from 550 to 750 nm (Figure 2g, J_{SC} = 27.70 mA cm⁻²) for the **PM6:YDF** based binary device. Thus, such significant OPV performance for **PM6:YTF**, **PM6:YTF-H**, and **PM6:YDF** warrants a systematic investigation.

Non-radiative Recombination Mechanism: The Influence of Dark state

We firstly measured the emission spectra of **YDF**, **YTF**, and **YTF-H** in dilute chloroform solution (Figure 3c), which have similar shapes to other NFAs having emission in the short-wavelength infrared region.^[29] The fluorescence peaks are almost the same for **YDF**, **YTF**, and **YTF-H** (~1.61 eV, 770 nm). The PLQY and transient absorption (TA) spectroscopy (Figure 4g) were carried out to investigate emission efficiency and exciton lifetime (τ) in three acceptors. As shown in Table S2, PLQY gradually decreased from 22.34% (**YDF**) to 0.84% (**YTF**) and 1.63% (**YTF-H**). Based on the equation of PLQY = $\frac{k_r}{k_r+k_{nr}} = \tau k_r$, the k_r and k_{nr} are 2.83 × 10⁸ and 1 × 10⁹, 5.25 × 10⁸, and 6.19 × 10¹⁰, and 8.80 × 10⁸ and 5.46 × 10¹⁰ s⁻¹ for **YDF**, **YTF**, and **YTF-H**, respectively. This implies the radiative rate is indeed increasing by spatially separating the HOMO-LUMO, but

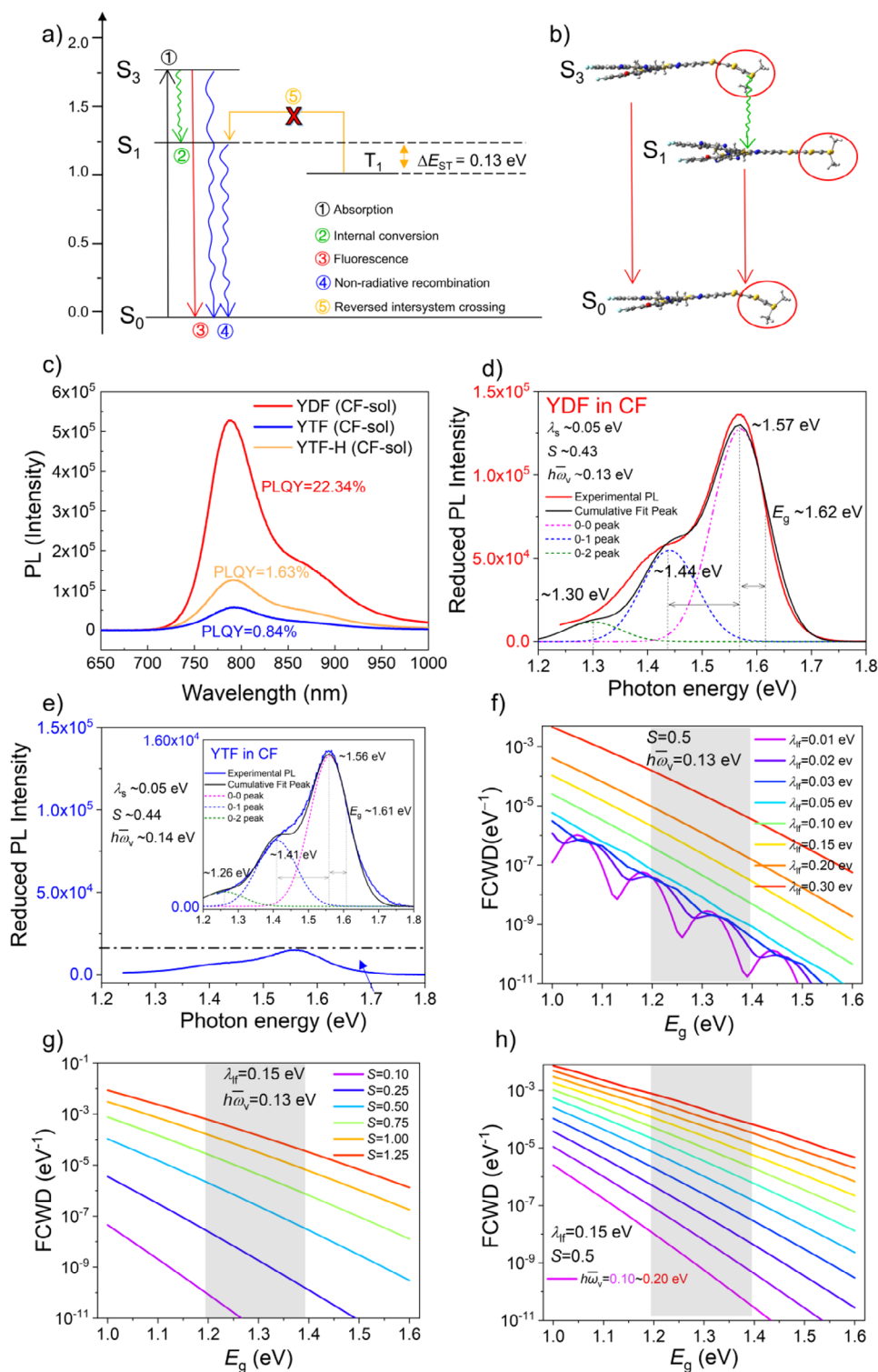


Figure 3. a) Illustration of excited-state dynamics in YTF: (1) photoexcitation of singlet states: optically bright transition characterized as local exciton $S_0 \rightarrow S_3$, $f = 1.78$; (2) IC: $S_3 \rightarrow S_1$; (3) fluorescence emission: $S_3 \rightarrow S_0$, $f = 1.79$; (4) non-radiative transitions of $S_3 \rightarrow S_0$ and $S_1 \rightarrow S_0$; (5) intersystem crossing. b) configurations of YTF at optimized S_0 , S_1 , and S_3 geometries. c) PL spectra and PLQY of the acceptors as extremely dilute solutions, excited at 600 nm. d) and e) the reduced photoluminescence spectra of solution fitted by multiple Gaussian peaks with equal width and spacing for acceptors. f)–h) dependence of FCWD on microscopic photophysical parameters.

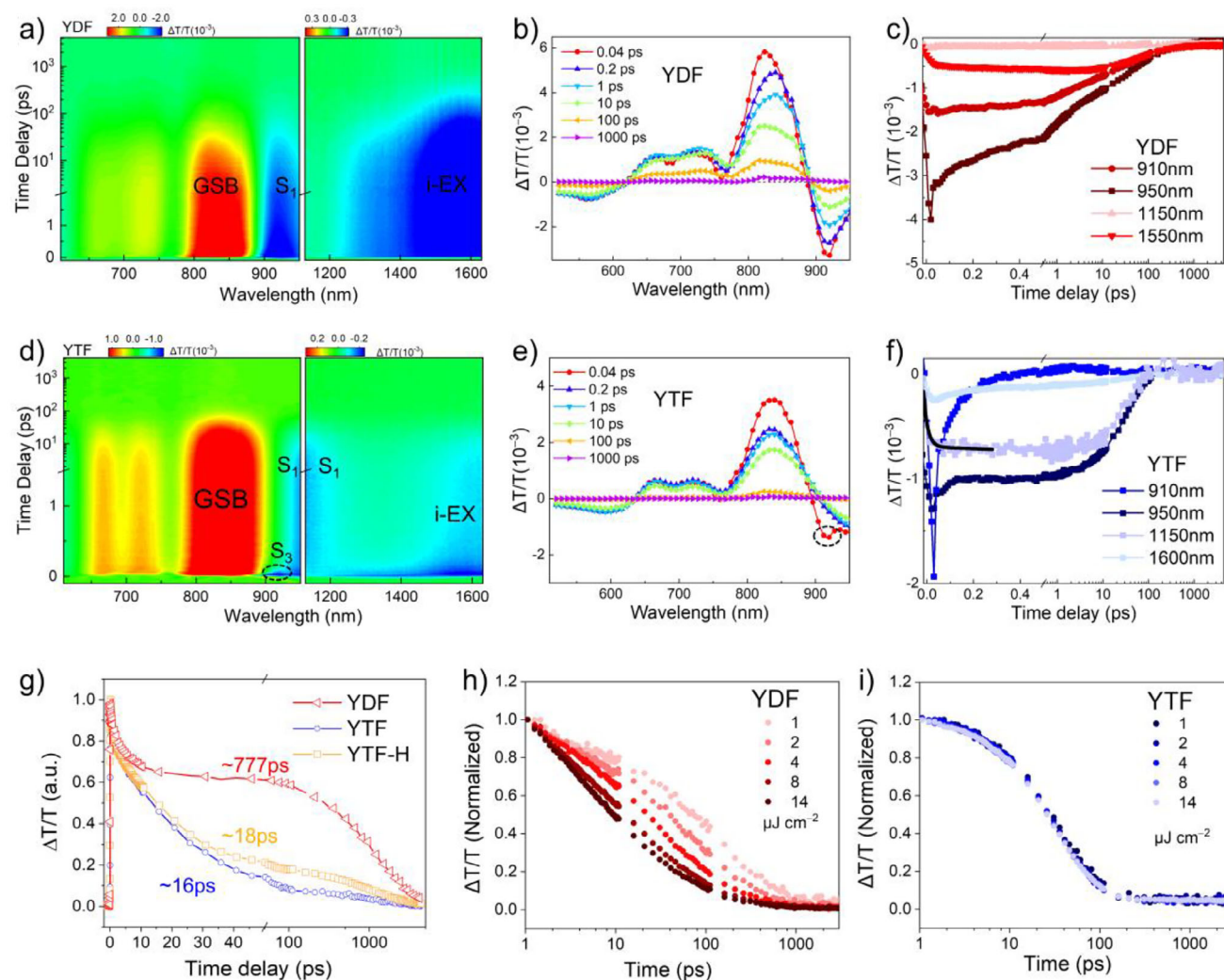


Figure 4. a), d) TA profiles of YDF and YTF neat film with pump at 750 nm. In YDF, the GSB band of YDF: 820 nm; The S_1 signals of YDF at 910 nm; the i-EX band of YDF: 1550 nm. In YTF, the GSB band of YTF: 820 nm; the S_3 signals of YTF: 910 nm; the S_1 signals of YTF: 950 ~ 1250 nm; the i-EX band of YTF: 1600 nm. b), e) TA spectra from the two samples at different time delays. c), f) The TA dynamics of ESA signals probed at 910 and 950 nm of YDF and YTF. g) The exciton lifetime of acceptors in dilute chloroform solution. h), i) Singlet-singlet exciton annihilation in neat YDF film and YTF film.

the non-radiative rate increases even more and dominates the process.

In order to understand the influence of electron-phonon coupling between the ground and excited states of this non-radiative process, wavefunction overlap between the vibrational levels of the excited and ground states for non-radiative recombination (Franck-Condon-weighted density; FCWD) is calculated by analyzing the fluorescence spectra, which could reflect the corresponding vibrational parameters (details in *Computational methods* of Supplementary). Consistent with the theoretically simulated absorption spectra discussed before, the similar fluorescence peaks indicate that the emission for YTF and YTF-H is contributed from the bright LE transition with strong oscillator strengths (Table S5). By investigating their similar reduced emission spectra (Figures 3b,c, and S14), oscillator strength, and FCWD, it could be concluded that YDF, YTF, and YTF-

H might present similar non-radiative channels accompanied by the fluorescence emission. However, the similar FCWD deduced from the reduced PL spectra could not be responsible for the large differences of PLQYs. It is thus possible that there is another important non-radiative process, which might be the dark $S_1 \rightarrow S_0$ transition (Figure 3a).

To our knowledge, generally the optically dark S_1 state does not contribute to the fluorescence emission but is largely involved in the non-radiative process.^[30] This situation makes it difficult to experimentally determine the excitation energy of the dark S_1 state. In order to estimate the FCWD of the $S_1 \rightarrow S_0$ non-radiative channel, we carried out a numerical simulation on the basis of Equation (S3). The influences of the aforementioned vibrational parameters and energy gaps are investigated in the range of various possible values (as shown in Figure 3f-h). It is obvious that the FCWD would significantly increase as reducing the E_g . Considering the

most likely range of E_g (~ 1.20 eV, the $\Delta E_{S_3-S_1}$ is estimated from the energy gap between CT and LE transition based on the results of CV measurement) and vibrational parameters ($\lambda_{if} \approx 0.15$ eV; $S \approx 0.5$; $h\bar{\omega}_v \approx 0.13$ eV), the *FCWD* of the dark $S_1 \rightarrow S_0$ non-radiative transition for **YTF** and **YTF-H** could be 4.01×10^{-7} eV $^{-1}$, which is almost five orders of magnitude larger than that of $S_3 \rightarrow S_0$ (1.67×10^{-11} eV $^{-1}$ for **YTF** and 1.84×10^{-12} eV $^{-1}$ for **YTF-H**, Table S4). It is thus rationalized that the lower-lying S_1 state provided an important non-radiative pathway interpreted in the energy gap law for **YTF** and **YTF-H**.

Therefore, it can be reasonably predicted that **YTF** and **YTF-H** possess an additional and dominant pathway contributing to the strong overall non-radiative recombination, potentially involving the $S_3 \rightarrow S_1 \rightarrow S_0$ transition (Figure 3a). This dominated non-radiative decay ($S_1 \rightarrow S_0$) significantly hinders the intersystem crossing (ISC) from S_1 to T_1 , making the ISC nearly impossible to occur, even with a ΔE_{ST} as low as ~ 0.1 eV.

To validate the results fitted by the experimental fluorescence spectra and the deduced optically dark state, we further carried out comprehensive theoretical calculations for **YDF**, **YTF**, and **YTF-H**. The geometries of both the ground and excited states were optimized; the vibrational parameters, energy gaps, and *FCWD* were all calculated and shown in (Table S4). The geometries of S_0 , S_1 , and S_3 present large differences around the C=C bonds in the TTF segment (Figure 3b and Tables S6–S10). For the non-radiative transition accompanied by the strong fluorescence emission ($S_1 \rightarrow S_0$ for **YDF** and $S_3 \rightarrow S_0$ for **YTF/YTF-H**), both the larger E_g and smaller electron-phonon coupling (especially the λ_{if} and S) lead to the reduced *FCWD*. For the specific $S_1 \rightarrow S_0$ non-radiative channel of **YTF/YTF-H**, in addition to the significant structural deformation (Figure 3b) contributing to the large electron-phonon coupling (Figure S4), the evidently reduced E_g dominates the *FCWD*, which is increased several orders of magnitude. Therefore, it could be concluded that the decreased energy of S_1 for **YTF/YTF-H** results in the prominent non-radiative recombination.

Excited State Dynamics

The dynamics of excitons and photocarriers in **YDF**, **YTF**, and **YTF-H** were then probed by the <20 fs TA spectroscopy. In dilute chloroform solution, **YDF** has a longer exciton lifetime of 777 ps, comparable with most excellent NFAs, but the exciton lifetime of **YTF** and **YTF-H** is one order of magnitude lower at 16 and 18 ps (Figure 4g), which should be caused by the serious non-radiation process as discussed above. No transition signal between excited states was observed in **YTF** and **YTF-H**, which may be attributed to the overlap of the excited state absorption (ESA) bands of S_1 and S_3 . Notably, the ground state bleaching (GSB) bands of **YTF** and **YTF-H** shifted from 766 to 750 nm within 2 to 50 ps, indicating that transitions between excited states (S_3 and S_1) occurred within this timeframe (Figure S32).

Within the ~ 1 ps time scale, the S_1 (Frenkel-type LE) state at 950 nm in the neat **YDF** film first emerges and then declines,

with the ESA bands at 1550 nm uprising, (Figure 4a–c) indicating fast conversion (<1 ps) of LE into an intermediate state. The ESA bands may correspond to an intermolecular i-EX state, where closely packed molecules help reduce exciton binding energy and facilitate the formation of excited species with CT characters.^[31]

In **YTF's** neat films, the ESA signal of the S_1 dark state was successfully captured. Simultaneously upon the optical pumping, the primary excitation of **YTF** is observed with ESA bands centered at 910 nm (S_3 state) and 1600 nm (i-EX state). At the same time, it can be clearly observed that compared with **YDF**, the i-EX and LE states of **YTF** have a significant decrease in the first 1 ps (Figure 4d). In addition, a feature ESA centered at 950–1250 nm appears upon optical pump and increases in the first 1 ps. As shown in Figure 4f, a transition signal from 910 to 1150 nm was observed, with a characteristic lifetime of approximately 0.06 ps, corresponding to a rate of around 10^{14} s $^{-1}$. This precisely matches the internal conversion (IC) process discussed above: the IC of **YTF** from S_3 to S_1 (dark state) after excitation.

In **PM6:YDF** film, after 10 ps, the ESA signals emerge at ~ 770 nm, which should be assigned to the charge separation (CS) state in the blend films, indicating the onset of the exciton dissociation. Simultaneously, the **YDF** blend gives a quick emergence of the bleach signal of **PM6**, indicating a hole transfer from acceptor to donor in **PM6:YDF** around 18 ps. Such a phenomenon was also observed in other highly performed OPVs.^[32,33] In the **YTF** blend film, it is clearly observed that S_1 acts as a trap state, capturing the energy of the S_3 excited state (Figure S38). For excitons that fall back to S_1 , severe non-radiative decay and the lack of driving force (due to the mismatch with the HOMO of **PM6**) prevent effective exciton dissociation. Consequently, a weak bleach signal near 630 nm persists on a much longer time scale of >2 ns, which represents a trace of hole transfer to **PM6**, corresponding to a current parameter of merely ~ 1.5 mA cm $^{-2}$. It is worth noting that even choosing the well-matched **PBDTTT-C-T** as a donor, excitons still fall back to the dark state and cannot be effectively dissociated, further supporting that S_1 is a trapped state (Figure S40).

The pump intensity dependent measurement further quantitatively supports this non-radiative process well, and it can be observed that compared with the strong pump intensity dependence of **YDF**, **YTF** has almost no pump dependence (Figure 4h,i). Different from the bimolecular recombination process of **YDF**, **YTF** showed a monomolecular recombination process. This shows that in the **YTF**-based system, **YTF** undergoes an extremely fast non-radiative process after being excited, which causes the excitons to be unable to diffuse effectively. In blends, this manifests as the inability of excitons to diffuse to the interface for effective separation, resulting in no charge generation.

Conclusion

In summary, a strategy for regulating the ΔE_{ST} for high performance OPV molecules by spatially separated HOMO and LUMO orbitals has been explored. By tuning the electron

donating characteristics of the central donor core unit, we achieved such a goal to regulate the spatial separation of HOMO and LUMO for molecules of **YDF**, **YTF**, and **YTF-H**. The optimized device based on **YDF** with partially HOMO and LUMO separation offers a high efficiency of 20.04%. But, for molecules of **YTF** and **YTF-H**, while they exhibit almost completely spatial HOMO–LUMO separation and much reduced ΔE_{ST} and also high electron mobility and absorption capacity, the much reduced ΔE_{ST} of **YTF** and **YTF-H** is mainly ascribed to the significantly decreased S_1 , which results in a marked enhancement of non-radiative processes caused by the energy-gap law and thus poor PCE of <1.5%.

The comprehensive analysis from simulation, photodynamic, spectroscopic, and crystallographic studies render us to propose the simultaneously required rules for an ideal OPV molecule: (1) A rigid and high aromatic conjugation system for strong light absorption and reduced electron-vibrational coupling; (2) Strong intermolecular interaction in the molecular packing for high charge mobility, such as currently used A-D-A molecules; (3) Small HOMO and LUMO overall integral through either spatially separated HOMO and LUMO or orthogonal HOMO and LUMO to reduce ΔE_{ST} . One optimized approach for the #3 requirement as demonstrated in this work is to raise the T_1 and ideally partially orthogonal HOMO and LUMO.

Acknowledgements

The authors gratefully acknowledge the financial support from the Ministry of Science and Technology of the People's Republic of China (National Key R&D Program of China, 2023YFE0210400) and the National Natural Science Foundation of China (52025033, 52373189, 21935007, 22361132530).

Conflict of Interests

The authors declare no conflict of interest.

Data Availability Statement

The data that support the findings of this study are available from the corresponding author upon reasonable request.

Keywords: Organic photovoltaic • Single-triplet energy gap • Nonradiative recombination • Energy gap law • High efficiency

- [1] Z. Chen, J. Ge, W. Song, X. Tong, H. Liu, X. Yu, J. Li, J. Shi, L. Xie, C. Han, Q. Liu, Z. Ge, *Adv. Mater.* **2024**, *36*, 2406690.
- [2] S. Guan, Y. Li, C. Xu, N. Yin, C. Xu, C. Wang, M. Wang, Y. Xu, Q. Chen, D. Wang, L. Zuo, H. Chen, *Adv. Mater.* **2024**, *36*, 2400342.
- [3] N. Wei, J. Chen, Y. Cheng, Z. Bian, W. Liu, H. Song, Y. Guo, W. Zhang, Y. Liu, H. Lu, J. Zhou, Z. Bo, *Adv. Mater.* **2024**, *36*, 2408934.

- [4] Z. Ge, J. Qiao, Y. Li, J. Song, X. Duan, Z. Fu, H. Hu, R. Yang, H. Yin, X. Hao, Y. Sun, *Angew. Chem. Int. Ed.* **2025**, *64*, e202413309.
- [5] H. Lu, D. Li, W. Liu, G. Ran, H. Wu, N. Wei, Z. Tang, Y. Liu, W. Zhang, Z. Bo, *Angew. Chem. Int. Ed.* **2024**, *63*, e202407007.
- [6] L. Zhu, M. Zhang, G. Zhou, Z. Wang, W. Zhong, J. Zhuang, Z. Zhou, X. Gao, L. Kan, B. Hao, F. Han, R. Zeng, X. Xue, S. Xu, H. Jing, B. Xiao, H. Zhu, Y. Zhang, F. Liu, *Joule* **2024**, *8*, 3153–3168.
- [7] Y. Sun, L. Wang, C. Guo, J. Xiao, C. Liu, C. Chen, W. Xia, Z. Gan, J. Cheng, J. Zhou, Z. Chen, J. Zhou, D. Liu, T. Wang, W. Li, *J. Am. Chem. Soc.* **2024**, *146*, 12011–12019.
- [8] C. Chen, L. Wang, W. Xia, K. Qiu, C. Guo, Z. Gan, J. Zhou, Y. Sun, D. Liu, W. Li, T. Wang, *Nat. Commun.* **2024**, *15*, 6865.
- [9] Y. Jiang, S. Sun, R. Xu, F. Liu, X. Miao, G. Ran, K. Liu, Y. Yi, W. Zhang, X. Zhu, *Nat. Energy* **2024**, *9*, 975–986.
- [10] K. Zhao, Q. Liu, L. Yao, C. Değer, J. Shen, X. Zhang, P. Shi, Y. Tian, Y. Luo, J. Xu, J. Zhou, D. Jin, S. Wang, W. Fan, S. Zhang, S. Chu, X. Wang, L. Tian, R. Liu, L. Zhang, I. Yavuz, H.-f. Wang, D. Yang, R. Wang, J. Xue, *Nature* **2024**, *632*, 301–306.
- [11] H. Chen, C. Liu, J. Xu, A. Maxwell, W. Zhou, Y. Yang, Q. Zhou, A. S. R. Bati, H. Wan, Z. Wang, L. Zeng, J. Wang, P. Serles, Y. Liu, S. Teale, Y. Liu, M. I. Saidaminov, M. Li, N. Rolston, S. Hoogland, T. Filleter, M. G. Kanatzidis, B. Chen, Z. Ning, E. H. Sargent, *Science* **2024**, *384*, 189–193.
- [12] H. Chen, Y. Zou, H. Liang, T. He, X. Xu, Y. Zhang, Z. Ma, J. Wang, M. Zhang, Q. Li, C. Li, G. Long, X. Wan, Z. Yao, Y. Chen, *Sci. China Chem.* **2022**, *65*, 1362–1373.
- [13] S. Liu, J. Yuan, W. Deng, M. Luo, Y. Xie, Q. Liang, Y. Zou, Z. He, H. Wu, Y. Cao, *Nat. Photonics* **2020**, *14*, 300–305.
- [14] Y. Kong, H. Chen, L. Zuo, *Adv. Funct. Mater.* **2025**, *35*, 2413864.
- [15] J. Wu, H. Cha, T. Du, Y. Dong, W. Xu, C. T. Lin, J. R. Durrant, *Adv. Mater.* **2022**, *34*, 2101833.
- [16] X.-K. Chen, D. Qian, Y. Wang, T. Kirchartz, W. Tress, H. Yao, J. Yuan, M. Hülsbeck, M. Zhang, Y. Zou, Y. Sun, Y. Li, J. Hou, O. Inganäs, V. Coropceanu, J.-L. Bredas, F. Gao, *Nat. Energy* **2021**, *6*, 799–806.
- [17] A. J. Gillett, A. Privitera, R. Dilmurat, A. Karki, D. Qian, A. Pershin, G. Londi, W. K. Myers, J. Lee, J. Yuan, S.-J. Ko, M. K. Riede, F. Gao, G. C. Bazan, A. Rao, T.-Q. Nguyen, D. Beljonne, R. H. Friend, *Nature* **2021**, *597*, 666–671.
- [18] A. Rao, P. C. Y. Chow, S. Gélinas, C. W. Schlenker, C.-Z. Li, H.-L. Yip, A. K. Y. Jen, D. S. Ginger, R. H. Friend, *Nature* **2013**, *500*, 435–439.
- [19] Y. Liu, C. Li, Z. Ren, S. Yan, M. R. Bryce, *Nat. Rev. Mater.* **2018**, *3*, 18020.
- [20] H. Uoyama, K. Goushi, K. Shizu, H. Nomura, C. Adachi, *Nature* **2012**, *492*, 234–238.
- [21] T. Hatakeyama, K. Shiren, K. Nakajima, S. Nomura, S. Nakatsuka, K. Kinoshita, J. Ni, Y. Ono, T. Ikuta, *Adv. Mater.* **2016**, *28*, 2777–2781.
- [22] T. Zhang, Y. Xiao, H. Wang, S. Kong, R. Huang, V. Ka-Man Au, T. Yu, W. Huang, *Angew. Chem. Int. Ed.* **2023**, *62*, e202301896.
- [23] L. Qin, X. Liu, X. Zhang, J. Yu, L. Yang, F. Zhao, M. Huang, K. Wang, X. Wu, Y. Li, H. Chen, K. Wang, J. Xia, X. Lu, F. Gao, Y. Yi, H. Huang, *Angew. Chem. Int. Ed.* **2020**, *59*, 15043–15049.
- [24] J. Yuan, Y. Zhang, L. Zhou, G. Zhang, H.-L. Yip, T.-K. Lau, X. Lu, C. Zhu, H. Peng, P. A. Johnson, M. Leclerc, Y. Cao, J. Ulanski, Y. Li, Y. Zou, *Joule* **2019**, *3*, 1140–1151.
- [25] Z. Yao, X. Wan, C. Li, Y. Chen, *Acc. Mater. Res.* **2023**, *4*, 772–785.
- [26] D. M. E. Freeman, A. J. Musser, J. M. Frost, H. L. Stern, A. K. Forster, K. J. Fallon, A. G. Rapisarda, F. Cacialli, I. McCulloch, T. M. Clarke, R. H. Friend, H. Bronstein, *J. Am. Chem. Soc.* **2017**, *139*, 11073–11080.

- [27] X.-K. Chen, D. Kim, J.-L. Brédas, *Acc. Chem. Res.* **2018**, *51*, 2215–2224.
- [28] Deposition numbers 2408868 (for **YTF**), 2408869 (for **YDF**) contain the supplementary crystallographic data for this paper. *These data are provided free of charge by the joint Cambridge Crystallographic Data Centre and Fachinformationszentrum Karlsruhe Access Structures service.*
- [29] Y. Xie, W. Liu, W. Deng, H. Wu, W. Wang, Y. Si, X. Zhan, C. Gao, X.-K. Chen, H. Wu, J. Peng, Y. Cao, *Nat. Photonics* **2022**, *16*, 752–761.
- [30] Y. Tu, J. Liu, H. Zhang, Q. Peng, J. W. Y. Lam, B. Z. Tang, *Angew. Chem. Int. Ed.* **2019**, *58*, 14911–14914.
- [31] R. Wang, C. Zhang, Q. Li, Z. Zhang, X. Wang, M. Xiao, *J. Am. Chem. Soc.* **2020**, *142*, 12751–12759.
- [32] L. Zhu, M. Zhang, J. Xu, C. Li, J. Yan, G. Zhou, W. Zhong, T. Hao, J. Song, X. Xue, Z. Zhou, R. Zeng, H. Zhu, C. C. Chen, R. C. I. MacKenzie, Y. Zou, J. Nelson, Y. Zhang, Y. Sun, F. Liu, *Nat. Mater.* **2022**, *21*, 656–663.
- [33] K. Jiang, J. Zhang, C. Zhong, F. R. Lin, F. Qi, Q. Li, Z. Peng, W. Kaminsky, S.-H. Jang, J. Yu, X. Deng, H. Hu, D. Shen, F. Gao, H. Ade, M. Xiao, C. Zhang, A. K. Y. Jen, *Nat. Energy* **2022**, *7*, 1076–1086.

Manuscript received: March 19, 2025

Revised manuscript received: June 25, 2025

Accepted manuscript online: June 30, 2025

Version of record online: July 14, 2025